

See discussions, stats, and author profiles for this publication at: <https://www.researchgate.net/publication/280966648>

# Photovoltaic performance and the energy landscape of CH<sub>3</sub>NH<sub>3</sub>PbI<sub>3</sub>

ARTICLE *in* PHYSICAL CHEMISTRY CHEMICAL PHYSICS · AUGUST 2015

Impact Factor: 4.49 · DOI: 10.1039/c5cp03352g · Source: PubMed

---

CITATIONS

2

---

READS

21

4 AUTHORS, INCLUDING:



Yecheng Zhou

University of Melbourne

15 PUBLICATIONS 160 CITATIONS

SEE PROFILE



Cite this: DOI: 10.1039/c5cp03352g

# Photovoltaic performance and the energy landscape of $\text{CH}_3\text{NH}_3\text{PbI}_3$ †

Yecheng Zhou,<sup>a</sup> Fuzhi Huang,<sup>b</sup> Yi-Bing Cheng<sup>b</sup> and Angus Gray-Weale<sup>\*a</sup>

Photovoltaic cells with absorbing layers of certain perovskites have power conversion efficiencies up to 20%. Among these materials,  $\text{CH}_3\text{NH}_3\text{PbI}_3$  is widely used. Here we use density-functional theory to calculate the energies and rotational energy barriers of a methylammonium ion in the  $\alpha$  or  $\beta$  phase of  $\text{CH}_3\text{NH}_3\text{PbI}_3$  with differently oriented neighbouring methylammonium ions. Our results suggest the methylammonium ions in  $\text{CH}_3\text{NH}_3\text{PbI}_3$  prefer to rotate collectively, and to be parallel to their neighbours. Changes in polarization on rotation of methylammonium ions are two to three times larger than those on relaxation of the lead ion from the centre of its coordination shell. The preferences for parallel configuration and concerted rotation, with the polarisation changes, are consistent with ferroelectricity in the material, and indicate that this polarisation is governed by methylammonium orientational correlations. We show that the field due to this polarisation is strong enough to screen the field hindering charge transport, and find this screening field in agreement with experiment. We examine two possible mechanisms for the effect of methylammonium ion rotation on photovoltaic performance. One is that rearrangement of methylammoniums promotes the creation and transport of charge carriers. Some effective masses change greatly, but changes in band structure with methylammonium rotation are not large enough to explain current–voltage hysteresis behaviour. The second possible mechanism is that polarization screens the hindering electric field, which arises from charge accumulation in the transport layers. Polarization changes on methylammonium rotation favour this second mechanism, suggesting that collective reorientation of methylammonium ions in the bulk crystal are in significant part responsible for the hysteresis and power conversion characteristics of  $\text{CH}_3\text{NH}_3\text{PbI}_3$  photovoltaic cells.

Received 10th June 2015,  
Accepted 28th July 2015

DOI: 10.1039/c5cp03352g

www.rsc.org/pccp

## 1 Introduction

A photovoltaic cell with a perovskite absorbing layer was first made by Kojima *et al.*<sup>1</sup> Highly efficient perovskite solar cells have been made,<sup>2–9</sup> and investigations of the mechanisms responsible for high efficiency continue.<sup>10–15</sup> Perovskite materials often exhibit ferroelectricity, and this behaviour has been reported in  $\text{CH}_3\text{NH}_3\text{PbI}_3$  ( $\text{MAPbI}_3$ ) thin films.<sup>16–18</sup> It is possible that the spontaneous polarisation affects a perovskite photovoltaic's performance. Polarisation effects in dye-sensitized solar cells (DSCs) and organic solar cells (OSCs) have been examined in detail, and it has been shown that polarization can improve their performance.<sup>19,20</sup> By introducing a permanent electric field in an ultra-thin layer of ferroelectric co-polymer at the interface between electrode and semiconductor layer of organic

solar cell, the interface charge can be decreased, and the Schottky barriers lowered, allowing increased charge collection efficiency and power conversion efficiencies (PCEs).<sup>21–23</sup> This evidence suggests that polarization may affect performance in perovskite cells also.

We use density functional theory (DFT) calculations to examine the mechanism of polarisation, particularly the tendency of methylammonium ( $\text{MA}^+$ ) ions to respond collectively, the relative energies of  $\text{MA}^+$  ions structures, and the heights of energy barriers between those structures. These reveal the energy landscape in which the disordered crystal moves in response to an electric field, and indicate a connection between the correlations and dynamics of  $\text{MA}^+$  ions, and a photovoltaic cell's performance and hysteresis characteristics. We report also the changes on polarisation in the creation and transport properties of electrons and holes, and discuss possible connections between polarisation and performance.

Among perovskites used as light absorbers in photovoltaic cells,  $\text{MAPbI}_3$  and  $\text{MAPbI}_x\text{Cl}_{3-x}$  are typical materials. At room temperature,  $\text{MAPbI}_3$  adopts a tetragonal structure, its  $\beta$ -phase. A transition to the cubic  $\alpha$ -phase takes place at 333 K.<sup>16</sup> Xing *et al.*<sup>24</sup> and Stranks *et al.*<sup>25</sup> have shown that these perovskite materials have very high electron–hole diffusion lengths from

<sup>a</sup> School of Chemistry, The University of Melbourne, Parkville, VIC, 3010, Australia.  
E-mail: angusg@unimelb.edu.au

<sup>b</sup> Department of Materials Science and Engineering, Monash University,  
Victoria 3800, Australia

† Electronic supplementary information (ESI) available: Band structure, DOS and Born charge. See DOI: 10.1039/c5cp03352g

100 nm to 1  $\mu\text{m}$ . A very wide absorption wavelength range with high incident photon-to-current efficiency (IPCE) has been observed by Burschka *et al.*<sup>3–5</sup> The structural and electronic properties of its  $\alpha$  phase have been discussed by the Aron group.<sup>10</sup> Zhao *et al.* have studied the orthorhombic perovskite  $\text{MAPbI}_3$  and they show that van der Waals (vdW) interactions are important in DFT calculations.<sup>26</sup> Du has discussed the electronic structure of the  $\beta$  phase of  $\text{MAPbI}_3$ , and reported small electron and hole effective masses, large Born effective charge, and benign traps and recombination centres, all of which contribute to exceptionally good carrier transport properties.<sup>27</sup> Frost *et al.* proposed that ferroelectric domains result in internal junctions, which promote the separation of excitons, and reduction of recombination through segregation of charge carriers.<sup>11,28</sup> The bulk photovoltaic effect related with ferroelectricity and ferroelectric domain wall have been discussed.<sup>29,30</sup> The links between these models and cell performance is not yet clear.

Hysteresis in current–voltage curves is seen in silicon solar cells, DSCs and OSCs at high scanning speeds.<sup>31–33</sup> This hysteresis is explained by capacitive charge, including space charges and trapped charges. When the scanning speed is faster than the release rate of traps, or faster than the space charge relaxation time, but not so fast that the charges cannot respond at all, hysteresis is seen.<sup>34</sup> In hybrid perovskite solar cells, hysteresis behaviours are much slower, but also more complex and anomalous. Most experiments on hybrid perovskite solar cells show stronger hysteresis when scanning speed increases,<sup>35–38</sup> but Snaith *et al.* also observed that slower scanning speed can lead to stronger hysteresis.<sup>39,40</sup> They attribute this anomalous hysteresis to a change to the nature of the electronic contact between the perovskite and the p- and n-type contact materials, which they verify by removing or changing the hole and electron transport layer. Tress *et al.* reported slow hysteresis, growing at slower scanning, in the photovoltaic absorbing layer without charge transport layers.<sup>14</sup> Some have focused on how to reduce or eliminate hysteresis by using a mixed solvent in the deposition process, increasing perovskite crystal size, and using mesoporous- $\text{TiO}_2$ .<sup>41,42</sup> We discuss here connections between the collective polarisation response of  $\text{MA}^+$  ions and normal or anomalous hysteresis.

To explain of the hysteresis effect in measurement of hybrid perovskite solar cells, several experiment have been set up. Tress *et al.* carried out a serial experiments and confirmed that there is a compensated field induced by some slow process. They think the ion migration is responsible for the slow process.<sup>14</sup> Zhang *et al.* showed that there is a field in the direction beneficial to charge collection in the solar cell and they believe this beneficial field is induced by the ionic motion.<sup>43</sup> Three mechanisms have been suggested for the photo-conductivity responses in ref. 44, they are the migration of the  $\text{MA}^+$  ions, photo-induced traps for charge carries in the  $\text{MAPbI}_3$  and the dipole alignment in the material. Their experiment of witnessing two opposite behaviours of decreased/increased photo-conductivity in the same material (different devices), makes the first two mechanisms less probable. Ion migration only can result in one response because ions always

migrate towards to the negative electrode. This dismisses the photo-induced traps as there is a increasing photo-conductivity over time. Here, by using theoretical methods, arguing from three points, we show that the polarisation of  $\text{MA}^+$  ions and perovskite unit cell are able to provide the compensated field observed in Tress's and Zhang's experiment. The first point is that the  $\text{MA}^+$  ions in its crystal can be reorientated by the operating field; the second point is that the rotatable ordered  $\text{MA}^+$  ions can provide overall polarisation; the point is that these polarized  $\text{MA}^+$  ions are able to provide a strong compensated field (In this paper, we call it the screening field), which promotes the charge transport and improves PCEs in perovskite solar cells.

We study both concerted and independent rotations of  $\text{MA}^+$  ions in  $\text{MAPbI}_3$ , and consider two possible mechanisms for the influence of polarisation on photovoltaic performance. One possible mechanism is that the polarisation by rearrangement of  $\text{MA}^+$  ions improves the electronic excitation properties of  $\text{MAPbI}_3$ , modifying the creation or transport of holes and conduction electrons. Under an external field, as that felt by the absorbing layer in an operating cell, the  $\text{MA}^+$  ions arrange in a preferred direction. With these ordered  $\text{MA}^+$  ions, the electronic structure is optimised. In this possible mechanism, for example, we might find the scattering by disorder in the lattice is minimized, hence, a small effective mass is expected.

The second possible mechanism is illustrated in Fig. 1, which shows the charge distribution in a normal solar cell without a screening medium (a), and a perovskite solar cell (b).

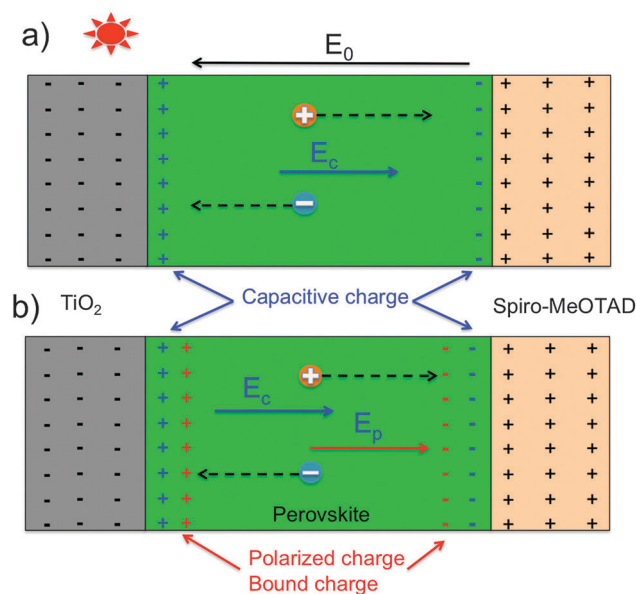


Fig. 1 The scheme of charge distribution in a normal solar cell without a ferroelectric medium (a), and a perovskite solar cell (b). The gray region on the left is the photo-anode. The excited electrons generated in the absorber layer (light green region in the centre) accumulate here. The dark green region on the right represent the photo-cathode, where holes accumulate.  $E_0$  is the hindering field. Capacitive charges are shown in blue. The field due to polarisation and the corresponding bound charges are shown in red.

The photo-anode is on the left. The excited electrons generated in the absorber layer accumulate here. The region on the right is the photo-cathode, where holes accumulate. Those accumulated charges in the charge transport layer build a potential difference, and so apply an electric field ( $E_0$ ) to the central, perovskite, absorbing layer. The direction of this electric field is from the photo-cathode to photo-anode. This field hinders the motion of electrons to the left, and holes to the right, therefore reducing performance. The energy level difference at the interfaces of anode/absorber and absorber/cathode also lead to charge accumulation, which act as capacitive charges (blue charges). This charge also will induce a field ( $E_c$ ), which will partly cancel the hindering field  $E_0$ . For a perovskite solar cell, the polarisation of the crystal can produce further bound charge at the interface (red charges). The field of these bound charges ( $E_p$ ) will further screen  $E_0$  and promote charge transport, and so improve performance. This possible mechanism is consistent with the compensated field in experiments.<sup>14,43</sup>

We first describe calculation methods, and then describe a representative selection of  $MA^+$  ions configurations, with their energies and band structures. We then describe Born effective charges, estimates of exciton energy, and polarisation changes on rotation of  $MA^+$  ions. Finally, we describe the energy barriers between the  $MA^+$  ion configurations studied, and discuss these in the context of measured hysteresis and performance characteristics of perovskite photovoltaics.

## 2 Calculation methods

The DFT calculations are performed by the Vienna Ab-initio Simulation Package (VASP),<sup>45,46</sup> which implements the projector augmented-wave (PAW) method<sup>47</sup> using a plane-wave basis set. The generalized gradient approximation (GGA) have been used to calculate the exchange correlations. Zhao *et al.* show that vdW interactions are important to DFT calculations on orthorhombic perovskite.<sup>26</sup> Giorgi *et al.* showed that hybrid methods applied on top of the spin-orbit coupling (SOC) calculated structures are not able to open the band gap sufficiently to reproduce the experimental value.<sup>48,49</sup> More advanced methods give improved results, for example GW + SOC calculations give the best agreement with experimental band gap at 1.5 eV.<sup>50</sup> The GW approximation (GWA) is an approximation made in order to calculate the self-energy of a many-body system of electrons by using the expansion of the self-energy in terms of the single particle Green's function  $G$  and the screened Coulomb interaction  $W$ . The GW + SOC method, shown to give the band structure closest to experiment, cannot feasibly be used with the nudged elastic band calculations that we use to map out the energy landscape of  $MAPbI_3$ . We exclude the GW method. In order to get relatively accurate results, we use GGA methods with or without considering the vdW interactions,<sup>51</sup> SOC or both of them. Very small band gaps calculated considering SOC in standard DFT do not agree with experiment, while the standard GGA gives band gap closer to experimental value.

We optimised the  $\beta$  phase of  $MAPbI_3$  with different methods, and then compared these obtained lattice parameters to experiment.

As shown in Table S6 (in ESI<sup>†</sup>), the sequence of lattice parameters and volumes estimated by various methods is: PBE > optPBE-vdW > optB86b-vdW > PBE-vdW > PBESol > Experimental > PBESol-vdW. The PBESol/GGA + vdW calculations will lead to cell vectors about 20% smaller than that in experiment. In general, for PBE/GGA calculations, vdW helps it to get more accurate lattice parameters. While for PBESol/GGA calculations, the implement of vdW interactions leads to inaccurate lattice parameters. Parameters calculated by PBESol are the closest parameters to experiment. Therefore, we chose the PBESol/GGA method without considering vdW interaction to calculate all the properties reported below.

The exchange correlation was calculated using the Perdew–Burke–Ernzerhof functional as revised for solids (PBESol).<sup>52</sup> The GGA PBESol calculations are done with the PBE–PAW potential considering 14 electrons  $5d^{10}6s^26p^2$  for lead. The pseudopotentials with  $5s^25p^2$ ,  $2s^22p^2$ ,  $2s^22p^3$  and 1s valence electrons are used for iodine, carbon, nitrogen and hydrogen, respectively. An energy cut-off was set at 500 eV. A  $\Gamma$ -centred Monkhorst mesh of  $9 \times 9 \times 9$  for the  $\alpha$  phase, and  $7 \times 7 \times 5$  for the  $\beta$  phase, was used for static calculations, including density of states (DOS) and band structure. For the band structure calculation, 60 points were inserted between each pair of high symmetry  $k$  points. The structures were optimized until the maximum force on each atom was smaller than  $0.01 \text{ eV } \text{\AA}^{-1}$ . For super-cells,  $3 \times 3 \times 3$   $\Gamma$ -centred Monkhorst mesh are used and the geometry were optimised until the force on each atom is smaller than  $0.02 \text{ eV } \text{\AA}^{-1}$ . At the beginning, we want to fully optimize the geometry of all the structure without any constraint, but we found that the optimized structure is not the same with the experiment. This because many local energy minimum configurations exist for  $MAPbI_3$ , while the phases that we interested are not stable at low temperature. Most of the optimised structures go to  $\gamma$  phase (the phase at lowest temperature) similar structures.<sup>16</sup> Here, we focus on the  $\alpha$  and  $\beta$  phase, as both and only  $\alpha$  and  $\beta$  phases are possible near room temperature. Therefore, we optimized the structures with the iodide ions fixed, while the shape and volume of cells allowed to change.

To get accurate second derivatives of energy, high-density points band-structure calculations have been performed. 60 points were used between each two high symmetry points. The second derivative was calculated as twice quadratic coefficient ( $a$ ) obtained by fitting. The fitting polynomial is,

$$E(\mathbf{k}) = a(\mathbf{k} - \mathbf{k}_0)^2 + c, \quad (1)$$

here  $E(\mathbf{k})$  is the energy and  $\mathbf{k}_0$  is the  $\mathbf{k}$  vector where its energy is the minimum (maximum) of the conduction (valence) band. Due to band crossing, the region over which the energy varies quadratically in  $\mathbf{k}$  is limited. This limits the data available for the determination of effective mass. Here, we use six points to fit the equation. In the absence of band crossing, the results are very similar for any number of points between 3 and 10.

The polarisation of the crystal and Born charges were calculated by Berry phase method, which is widely used to analyse the polarisation in crystal.<sup>53–56</sup> The dielectric constant

is estimated by means of density functional perturbation theory.<sup>57</sup> The nudged elastic band (NEB) is a method used to find the minimum energy reaction paths (MEP) when both of the initial and final states are known. It has been implemented in VASP.<sup>58</sup> First, linearly interpolating a set of structures between the known initial and final states gives an initial guess for the path. The energy of this string of images is then minimised. Thus the MEP is revealed. A refined climbing image NEB method calculates not only MEP but also the saddle point. It drives the image with the highest energy up to the saddle point. The force at this saddle point along the tangent changes sign. In this way, the image tries to maximize its energy along the band, and minimize in all other directions. When this image converges, it will be at the exact saddle point.<sup>59</sup> In this paper, the energy barrier for MA<sup>+</sup> ions rotations are performed by climbing image NEB (cNEB) calculations. In searching for the saddle points, the relaxation is stopped if all forces are smaller than 0.05 eV Å<sup>-1</sup>.

### 3 Results and discussion

We set out here the properties of structures of the  $\alpha$  and  $\beta$  phases, and most importantly, the energy barriers between these states. In this part, we will examine two possible mechanisms for the PCE performance and three points for the explanation of hysteresis we have suggested above.

#### 3.1 Structures and energies

The MAPbI<sub>3</sub> crystal includes an inorganic lead and iodide framework and MA<sup>+</sup> ions. The disordered MA<sup>+</sup> ions are associated with the cage of Pb–I atoms as reported in X-ray diffraction.<sup>60–62</sup>

Due to weak interaction between MA<sup>+</sup> ions and the inorganic frame, multiple local energy minimum structures exist. MA<sup>+</sup> ions may point in different directions. In previous theoretical studies, MA<sup>+</sup> ions are oriented to different directions in orthorhombic,<sup>26,63,64</sup> cubic,<sup>10,12,48</sup> or tetragonal structure,<sup>27,50</sup> which leads to different results, such as band gap, and effective mass. Here we systematically compare three representative structures with differently oriented MA<sup>+</sup> ions, in both the  $\alpha$  and  $\beta$  phases. The MA<sup>+</sup> ion oriented along [001] direction is denoted 100-MAPbI<sub>3</sub> (Fig. 2(a) and (d)), in which MA<sup>+</sup> ion (C–N bond) is parallel to  $c$  axis. The other two cases are MA<sup>+</sup> ion oriented to [110] (110-MAPbI<sub>3</sub>, Fig. 2(b)) and [111] (111-MAPbI<sub>3</sub>, Fig. 2(c)). The unit cell of the  $\beta$  phase has four MA<sup>+</sup> ions, we start energy minimisations with all of the MA<sup>+</sup> ions oriented to [001], [110] and [111]. These oriented MA<sup>+</sup> ions change their orientations little on energy minimisation. Two different methods have been used to optimize its structure. The first method keeps the inorganic component fixed during geometry optimisation; another method keeps the iodide ions fixed, while relaxing lead ions and MA<sup>+</sup> ions. For  $\alpha$  phase, the 111-MAPbI<sub>3</sub> always has the lowest energy (Table 1). The energy differences between structures are about 10 meV for the  $\alpha$  phase, so that, barriers permitting, MA<sup>+</sup> ions are able to rotate at room temperature. This difference becomes about 100 meV (25 meV for each MA<sup>+</sup> ion) in the  $\beta$  phase, so that it is a little less thermodynamically favoured for MA<sup>+</sup> ions to rotate in  $\beta$  phase than that in  $\alpha$  phase, but still possible.

#### 3.2 Band structure of MAPbI<sub>3</sub>

Borriello *et al.* have shown that the electronic properties of tin-halide perovskitic compounds are strongly dependent on the

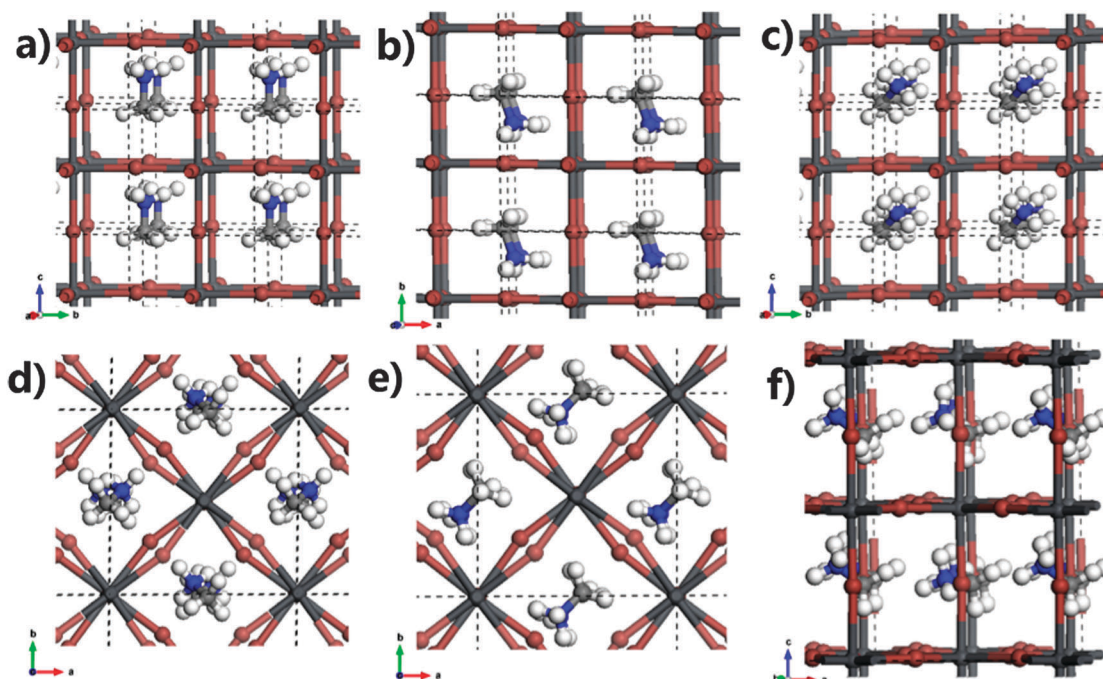


Fig. 2 The optimized structure of MAPbI<sub>3</sub> with lead ions fixed, MA<sup>+</sup> were initially oriented along direction (a) [001]; (b) [110]; (c) [111] in  $2 \times 2 \times 2$  super cells of  $\alpha$  phase. The unit cell of  $\beta$  phase with MA<sup>+</sup> were initially oriented along direction (d) [001]; (e) [110]; (f) [111] in a single unit cell. The carbon and nitrogen coordination difference was defined as the direction. The dash brown lines are the boundaries of unit cells.



**Table 1** The energies of MAPbI<sub>3</sub> with various MA<sup>+</sup> orientations with or without lead atom relaxed. Structures show in Fig. 2

Phase	Orientation	Lead relaxed (eV)	Lead fixed (eV)
$\alpha$	001	-52.046	-52.046
	110	-52.054	-52.051
	111	-52.060	-52.059
$\beta$	00 $\bar{1}$	-208.724	-208.360
	$\bar{1}\bar{1}0$	-208.551	-208.338
	$\bar{1}\bar{1}1$	-208.689	-208.328

structure of the inorganic cage, as the valence and conduction bands are dominated by the inorganic cage.<sup>65</sup> This view is confirmed with our calculation that the band gaps with differently oriented MA<sup>+</sup> ions are similar, but we found that the shape at the bottom and top of the conduction and valence band changes as the MA<sup>+</sup> ion rotates. The band structure of the  $\alpha$  and  $\beta$  phases, with lead relaxed, are shown in Fig. 3. The band gaps are about 1.2 eV ( $\alpha$  phase) and 1.3 eV ( $\beta$  phase), due to the normal DFT underestimation of band gaps, these are lower than the experimental value of 1.5 eV.<sup>60</sup> There is little difference among those structures with differently oriented MA<sup>+</sup> ions. In the  $\alpha$  phase, the band gap of 110-MAPbI<sub>3</sub> (1.21 eV) is smaller than that of 001- (1.24 eV) and 111-MAPbI<sub>3</sub> (1.29 eV). The band gaps for the structures optimized with lead fixed are 1.22 eV, 1.15 eV, and 1.26 eV for 001-, 110- and 111-MAPbI<sub>3</sub>, shown in Fig. S1 (ESI<sup>†</sup>).

The band structures of the  $\beta$  phase are shown at the bottom of Fig. 3. Band gaps are 1.42 eV, 1.30 eV, 1.27 eV for 001-, 110- and 111-MAPbI<sub>3</sub>. They are 1.39 eV, 1.28 eV and 1.31 eV for lead-relaxed 001-, 110- and 111-MAPbI<sub>3</sub>. The band gaps of the structure with lead fixed are about 3% different from that of

the lead relaxed  $\beta$  phase, shown in Fig. S1 (ESI<sup>†</sup>). Those theoretical band gaps are close to the experimental value of 1.5 eV.<sup>60</sup> The electron DOS is shown in Fig. S2 (ESI<sup>†</sup>). The band divergence of different oriented MA<sup>+</sup> ions agrees with Brivio's work on the  $\alpha$ -phase.<sup>10</sup>

We find that orientation of MA<sup>+</sup> ions has a relatively weak effect on the band gap, too small to have any significance consequences for photovoltaic performance. Hence, the first suggested mechanism, is not indicated.

### 3.3 The effective masses

We estimate the effective mass based on its definition,

$$\frac{1}{m^*} = \frac{1}{\hbar} \frac{d^2 E(\mathbf{k})}{d\mathbf{k}^2}, \quad (2)$$

where the  $E(\mathbf{k})$  is the energy of a band and  $\mathbf{k}$  is the wave vector. The method to calculate the second derivative of energy we have illustrated in the Method.

For the  $\alpha$  phase, estimated masses are shown in Table 2. The effective hole masses are about  $0.16m_0$ . This hole effective mass in changes as the MA<sup>+</sup> ion rotates by about 10%. For electron transport, effective masses are anisotropic, and individual values differ greatly between different MA<sup>+</sup> ion orientations. There are three conduction bands with very little energy difference, which suggests all of them could contribute to charge transport. The harmonic mean electron effective masses are  $0.174m_0$ ,  $0.180m_0$  and  $0.171m_0$  for [001], [110] and [111], respectively.

The extrema of band structure are at the  $\Gamma$  point in the  $\beta$  phase. For hole transport, effective masses differ little among reciprocal space directions, and vary little as the MA<sup>+</sup> ion rotates. We find again in the  $\beta$  phase anisotropic band structure for

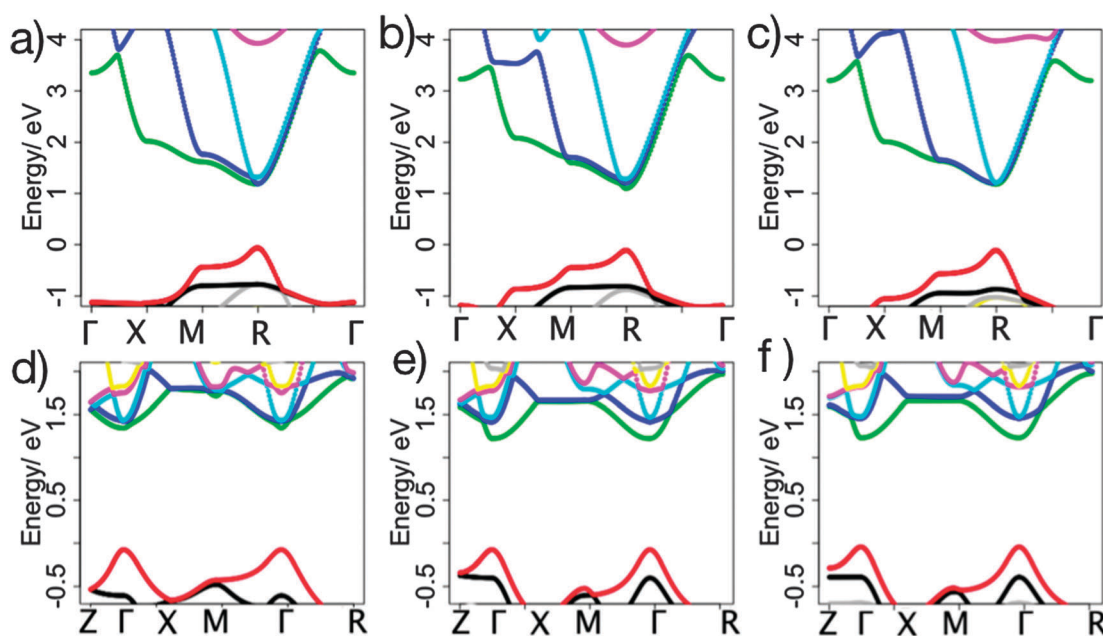


**Fig. 3** The band structure of  $\alpha$  phase and  $\beta$  phase optimized with lead relaxed. The (a), (b) and (c) are the band diagrams of  $\alpha$  phase, corresponding to 001-, 110- and 111-MAPbI<sub>3</sub>, respectively. The band diagrams of  $\beta$  phase are shown as (d), (e) and (f) corresponding to 001-, 110- and 111-MAPbI<sub>3</sub>, respectively.

**Table 2** Effective hole and electron masses of the  $\alpha$  phase with lead atoms relaxed. These results were fitted with 6 points near the  $R$  point. The effective mass unit is  $m_0$  (the static mass of a free electron)

MA <sup>+</sup> orientation	Bands	$M-R$	$R-\Gamma$	Harmonic mean
001	VB	−0.172	−0.149	−0.160
110		−0.197	−0.154	−0.173
111		−0.150	−0.144	−0.147
001	CB1	0.325	0.156	0.174
	CB2	0.079	0.176	
	CB3	0.655	0.198	
110	CB1	0.402	0.155	0.180
	CB2	0.223	0.179	
	CB3	0.106	0.207	
111	CB1	0.069	0.129	0.171
	CB2	1.044	0.192	
	CB3	0.480	0.219	

electron transport. The electron effective masses are very sensitive to the direction of the crystal momentum  $\mathbf{k}$ . For the first conduction band in the  $\beta$  phase (the lowest energy conduction band), they have very small effective masses (lighter than  $0.1m_0$ ) in the direction of the  $Z$  point. While the band bottom becomes very flat in the direction of the  $X$  point, especially for the 100- and 111-perovskite (Table 3). Due to its highly anisotropic transport properties, we also calculated the effective masses in the directions of other high symmetry  $\mathbf{k}$  points, as shown in Table 3. The calculated effective masses are about  $0.1m_0$ . The inequivalence of the  $M$  and  $M_2$  points for the configuration  $[00\bar{1}]$ , is due to symmetry breaking by the hydrogen atoms, and the MA<sup>+</sup> ion not aligning exactly in the direction of  $[00\bar{1}]$ . The harmonic mean electron effective masses are  $0.199m_0$ ,  $0.192m_0$  and  $0.195m_0$  for  $[00\bar{1}]$ ,  $[110]$  and  $[111]$  directions, respectively.

We find effective masses for some one-electron states are very sensitive to the orientations of MA<sup>+</sup> ions, while the harmonic

**Table 3** Effective hole and electron masses of the  $\beta$  phase along with different directions with lead relaxed. These results were fitted with 6 points near the  $\Gamma(0, 0, 0)$  point. The effective mass unit is  $m_0$ . The directions in  $\mathbf{k}$ -space are:  $M(0.5, 0.5, 0)$ ,  $R(0.5, 0.5, 0.5)$ ,  $Z(0, 0, 0.5)$ ,  $X(0, 0.5, 0)$ ,  $M_2(0.5, -0.5, 0)$ ,  $R_2(0.5, 0.5, -0.5)$

MA <sup>+</sup> direction	Band	$Z-\Gamma$	$\Gamma-X$	$M-\Gamma$	$\Gamma-R$	$M_2-\Gamma$	$\Gamma-R_2$	Harmonic mean
00 $\bar{1}$	CB3	0.08	0.12	0.15	0.15	0.07	0.14	0.199
	CB2	0.22	0.74	0.71	0.60	3.22 <sup>a</sup>	0.51	
	CB1	1.28	0.23	0.18	0.15	0.93	0.20	
	Mean <sup>b</sup>	0.53	0.36	0.35	0.30	1.41	0.28	
110	CB3	0.73	0.10	0.08	0.10	0.09	0.10	0.192
	CB2	0.89	0.18	0.45	0.51	0.30	0.50	
	CB1	0.07	1.81	1.40	0.29	1.49	0.34	
	Mean <sup>b</sup>	0.56	0.70	0.64	0.30	0.63	0.31	
111	CB3	0.78	0.11	0.08	0.10	0.08	0.10	0.195
	CB2	1.01	0.18	0.62	0.67	0.62	0.67	
	CB1	0.07	1.02	0.94	0.29	0.95	0.29	
	Mean <sup>b</sup>	0.62	0.44	0.55	0.35	0.55	0.35	

<sup>a</sup> Is the effective masses calculated from fitting to 10 points around the numerically determined minimum just off the  $\Gamma$  point. <sup>b</sup> Is the harmonic mean.

mean effective hole masses vary little. This raises the possibility that in certain directions in the  $\beta$ -phase, for one electron states, the electron mobility responds strongly to polarisation. But overall the effective masses and mobility do not much differ. Therefore, the first possible mechanism for high PCEs is less probable.

### 3.4 Born effective charge

For the lead atoms in both the  $\alpha$  and  $\beta$  phases, the diagonal elements are close to  $4.6e$ , where  $e$  is the magnitude of the elementary charge, while the non-diagonal elements are smaller than  $0.5e$ . In optimized structures, the MA<sup>+</sup> ions are not at the centre of inorganic cages, carbon atoms of MA<sup>+</sup> ions are always closer to the cage boundary. The  $zz$  component of the Born charge of the lead atom reduces from  $5.15e$  to  $5.01e$  to  $4.78e$ , as MA<sup>+</sup> ion rotate from  $[001]$  to  $[101]$  and to  $[111]$  for the  $\alpha$  phase, as shown in Table 4. Carbon atoms are strongly coupled to the lead ions. The Born charges of iodide ions are dependent on their position and coordination geometry around the lead atoms. In the  $\alpha$  phase, the iodide Born charge is about  $-4.5e$  in the Pb–I bond direction, and almost zero in other directions. The trends are similar in the  $\beta$  phase, but two types of iodides are present: one is apical, located at the center of two lead ions, the other is equatorial.<sup>27</sup> The apical iodides behave as in the  $\alpha$  phase, but for the equatorial iodides, the Born charges in the plane of its two Pb–I bonds are about  $-2.6e$ , the direction out of plane is very small. More Born charges of the  $\alpha$  and  $\beta$  phases are listed at Tables S2–S5 (ESI<sup>†</sup>). The Born effective charges are roughly twice as large as the corresponding formal charge ( $2.0e$ ). The large Born effective charges are related to the large static dielectric constant, or the ferroelectric character, as appropriate. The large dielectric constant and the resulting screening of defects and impurities may promote transport properties.<sup>27,66</sup> These results show modest changes in the behaviour of the electrons in the inorganic framework with MA<sup>+</sup> ions rotation. That argues for the importance of the ‘macroscopic’ mechanism of Fig. 1 over the possibility of changes in electronic structure with MA<sup>+</sup> ion rotation.

### 3.5 Exciton separation energy

The energy needed for exciton separation is the energy difference between the lowest and highest energy levels of the two-charge

**Table 4** Born charge of the lead ions in  $\alpha$  phase. It varies as the MA<sup>+</sup> ion vectors

MA <sup>+</sup> orientation	Direction	$X$	$Y$	$Z$
[001]	$X$	4.688	0.007	−0.064
	$Y$	0.007	4.682	−0.060
	$Z$	−0.063	−0.059	5.146
[101]	$X$	4.995	0.007	−0.030
	$Y$	0.008	4.515	0.360
	$Z$	−0.030	0.372	5.010
[111]	$X$	4.863	0.021	0.072
	$Y$	0.021	4.882	0.073
	$Z$	0.071	0.073	4.776

**Table 5** Dielectric tense including local field effects in DFT for the  $\alpha$  and  $\beta$  phases with representative the  $\text{MA}^+$  ion orientations

$\text{MA}^+$ orientation	Direction	$X$	$Y$	$Z$
$\alpha[001]$	$X$	5.90	−0.00	0.01
	$Y$	−0.00	5.88	0.02
	$Z$	0.01	0.02	6.26
$\alpha[110]$	$X$	6.20	−0.00	−0.01
	$Y$	−0.00	5.73	0.19
	$Z$	−0.01	0.19	6.21
$\alpha[111]$	$X$	5.74	0.06	0.08
	$Y$	0.06	5.74	0.07
	$Z$	0.08	0.07	5.70
$\beta[001]$	$X$	5.70	−0.03	0.04
	$Y$	−0.03	5.70	0.04
	$Z$	0.04	0.04	6.97
$\beta[110]$	$X$	5.95	0.06	0.09
	$Y$	0.06	5.95	−0.09
	$Z$	0.09	−0.09	6.49
$\beta[111]$	$X$	5.90	0.00	−0.10
	$Y$	0.00	5.88	−0.05
	$Z$	−0.10	−0.05	6.78

system. The  $n$ th orbital energy of two-charge system is,

$$E_n = -\frac{1}{n^2} \left( \frac{e^2}{4\pi\epsilon\epsilon_0} \right)^2 \frac{m_{\text{ex}}}{2\hbar^2} + \frac{\hbar^2 \mathbf{k}^2}{2M}, \quad (3)$$

where  $m_{\text{ex}} = \frac{m_e \times m_h}{m_e + m_h}$ ,  $M = m_e + m_h$ , where,  $m_e$  and  $m_h$  are the effective electron and hole masses.  $\hbar$  is the reduced Plank constant,  $\epsilon$  is the relative dielectric constant and  $\epsilon_0$  is the vacuum permittivity. The last term is the kinetic energy of the exciton. The first term is the orbital energy of different states. The maximum energy for charge separation is to excite a two-charge system from the ground state ( $n = 1$ ) to the highest excited state ( $n = \infty$ ). For  $\text{MAPbI}_3$  the harmonic mean effective hole and electron masses are about  $0.16m_0$  and  $0.20m_0$  (shown in Tables 2 and 3), respectively, and the static dielectric constant describing the response of the electrons with ions fixed is about 6.0, shown in Table 5, calculated from density functional perturbation theory. Using those parameters, we estimated the binding energy to be 30 meV, which agrees with experiment (37 meV,<sup>67</sup> 45 meV<sup>68</sup> and 50 meV<sup>69</sup>). The reduced mass ( $m_{\text{ex}}$ ) calculated from our *ab initio* calculation is  $0.09m_0$ , close to the experimental value ( $0.12m_0$ ,<sup>67</sup>  $0.11m_0$ ,<sup>68</sup> and  $0.15m_0$ <sup>69</sup>). The small exciton separation energy will promote charge separation, and increase their solar cell's working current.

The static dielectric constant, and effective mass averaged over different directions change little on rotation of the  $\text{MA}^+$  ion, so we expect little change in the exciton binding energy across the energy landscape. More importantly, our results are consistent with experimental evidence that the formation of excitons is not a significant performance limiting process.

### 3.6 Polarisation due to motion of the lead ions

A typical perovskite material has a formula expressed as  $\text{ABX}_3$ . B is the atom at the centre of octahedron, whose movement is

**Table 6** The lead ions displacement ( $\Delta\mathbf{r}$ ) and the dipole moment differences ( $\Delta\mathbf{M}$ ) between the structures with or without lead ion relaxed for  $\beta$  phase  $\text{MAPbI}_3$ 

Initial $\text{MA}^+$ orientation	$\Delta\mathbf{r}$ (Å)	$\Delta\mathbf{M}$ (e Å)	$ \Delta\mathbf{P} $ ( $\mu\text{C cm}^{-2}$ )
$\beta[001]$	(0.15, 0.20, 0.07)	(−0.01, 0.18, −1.86)	3.0
$\beta[\bar{1}\bar{1}0]$	(0.04, 0.18, 0.15)	(−0.70, −1.11, −0.65)	2.3
$\beta[\bar{1}\bar{1}1]$	(0.21, 0.07, −0.02)	(−1.03, −0.47, −0.86)	2.3

usually considered as the mechanism of polarisation for a ferroelectric perovskite. For  $\text{MAPbI}_3$ , B is the lead ion. First, we discuss the possible polarisation due to lead atoms, which is estimated from the change in dipole moment of the unit cells as the lead atom relaxes from the centre of its iodide coordination octahedron. The energy of the relaxed structure is slightly lower than that of the structure with lead fixed. Table 6 shows the average displacement of the four lead atoms and the dipole moment difference between the geometry with or without lead atom relaxed in the  $\beta$  phase  $\text{MAPbI}_3$ , with different  $\text{MA}^+$  ion orientations. The polarisation change on relaxation of the lead ions is roughly a half or a third of that obtained by rotation of  $\text{MA}^+$  ions (see below). There is no obvious relation between the polarisation direction and the average lead atoms displacement. This effect is due to the coupling of  $\text{MA}^+$  ions to the inorganic component of the crystal.

### 3.7 Polarisation due to rotation of the $\text{MA}^+$ ion

The  $\text{MA}^+$  ion has dipole moment in the gas phase of 2.29 Debye,<sup>11</sup> and we can not rule out the possibility that the crystal polarisation is mainly contributed by the  $\text{MA}^+$  ion. To study its polarisation properties, the Berry phase of those crystals with differently oriented  $\text{MA}^+$  ions have been investigated. Table 7 shows the dipole moments of those unit cells. In this part of calculation lead atoms are fixed in order to eliminate their influence. As the four  $\text{MA}^+$  ions are on the boundary of the  $\beta$  phase unit cell, to calculate the dipole moment change, we need to chose a boundary not crossed by an ion. Generally, if we select a centre so that there is not much electron cloud or ions crossing the cell's boundary, the dipole moment change of the cell is proportional to change in the  $\text{MA}^+$  ion carbon–nitrogen bond vector. As shown in Table 4 the Born charges on the inorganic frame change as the  $\text{MA}^+$  ion rotates. This coupling between inorganic and  $\text{MA}^+$  ions make it impossible to get a perfect linear relationship between the  $\text{MA}^+$  ion orientations

**Table 7** Average  $\text{MA}^+$  ions vector changes ( $\Delta\mathbf{r}$ ) and dipole moment difference ( $\Delta\mathbf{M}$ ) for the  $\beta$  phase  $\text{MAPbI}_3$ ,  $\text{MA}^+$  ion orientating from  $[\bar{1}\bar{1}0]$  or  $[\bar{1}\bar{1}1]$  to  $[001]$ 

Initial $\text{MA}^+$ orientation	$\Delta\mathbf{r}$ (Å)	$\Delta\mathbf{M}$ (e Å)	$ \Delta\mathbf{P} $ ( $\mu\text{C cm}^{-2}$ )
$[\bar{1}\bar{1}0]^a$	(−0.94, −0.32, 1.19)	(1.43, −1.44, −3.44)	6.40
$[\bar{1}\bar{1}1]^b$	(−1.02, 0.22, 1.84)	(2.12, 0.49, −4.54)	8.06

<sup>a</sup> Calculated with centre at (0.35, 0.86, 0.50). <sup>b</sup> Calculated with centre at (0.35, 0.85, 0.50).



and the dipole moments of their unit cells. The polarisation induced by the  $\text{MA}^+$  ion rotation is two or three times larger than the polarisation induced by the lead atom. Therefore, we can draw a conclusion that the polarisation of  $\text{MAPbI}_3$  is controlled by the  $\text{MA}^+$  ions, but the coupling between the two is strong, and the role of the inorganic frame cannot be neglected. This is the second point of the argument that the rotation of  $\text{MA}^+$  is able to polarise the material.

### 3.8 Barriers to methylammonium ions rotation

The direction of spontaneous polarisation in a ferroelectric depends not only on the field but also on the history of the material. The properties of a ferroelectric material develop on cooling the dielectric phase towards the ferroelectric transition temperature, with a diverging correlation length for ferroelectric order. We might therefore expect to see collective orientation of the  $\text{MA}^+$  ions favoured in the  $\alpha$  phase, and consider that structure first.

The energy differences between structures in the energy landscape with differently oriented  $\text{MA}^+$  ions are about the thermal energy at room temperature (25 meV), so  $\text{MA}^+$  ions can rotate at room temperature (see Fig. 4 and Table 1). If the energy barrier for a rotating  $\text{MA}^+$  ion is high, the rotation will be slow, and then the polarisation of  $\text{MA}^+$  ion cannot in a practical period of time be tuned by external electric field. To determine the energy barrier for  $\text{MA}^+$  ion reorientation, cNEB calculations have been performed.<sup>59</sup> We estimated energy barriers for the  $\text{MA}^+$  ion rotated between [001], [110] and [111] directions in  $\alpha$  phase. The  $\alpha$  phase unit cell only has one  $\text{MA}^+$  ion. When it rotates, the neighbouring  $\text{MA}^+$  ions in the periodic images of the cell are also rotated. For  $\alpha$  phase, the energy barrier is about 14 meV for a  $\text{MA}^+$  ion rotates between [001] and [011], which is lower than  $kT$ . The largest energy barrier is for [111]- $\text{MA}^+$  ion rotation to [001] or [011] direction, 82 meV or 98 meV, respectively, shown in Fig. 4. Even the largest energy barrier is only four times higher than  $kT$ , so the  $\text{MA}^+$  ions can rotate collectively at room temperature.

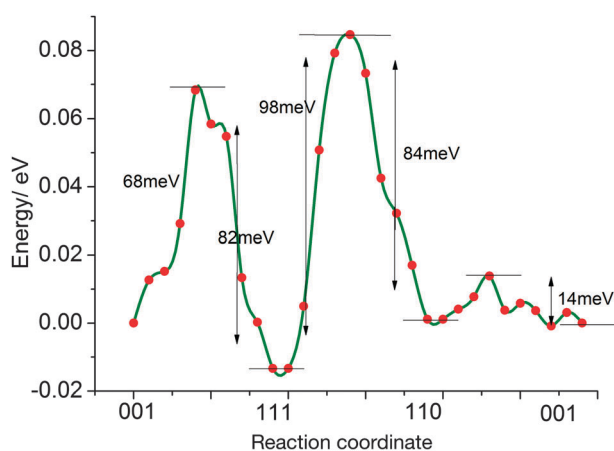


Fig. 4 The energy landscape of  $\text{MA}^+$  ion rotates in representatives orientations in the  $\alpha$  unit cell.

Ferroelectric response favours collective polarisation, and so we calculate also the energy barrier to reversal of orientation of a single  $\text{MA}^+$  ion with either its neighbours fixed or moving in parallel. This comparison is shown for both the  $\alpha$  and  $\beta$  phases in Fig. 5. We choose the  $\text{MA}^+$  ion rotation from [001] to [00 $\bar{1}$ ]. For the  $\alpha$  phase, the collective energy barrier for one  $\text{MA}^+$  ion is 74 meV, as shown in Fig. 5(b). For independent rotation, the barriers are about zero if the start  $\text{MA}^+$  ion configuration anti-parallel to surrounding  $\text{MA}^+$  ions, where the reaction coordinate  $\approx 12$  Å. If  $\text{MA}^+$  ion starting configuration is parallel to surrounding  $\text{MA}^+$  ions (reaction coordinate  $\approx 0$  Å), the barrier is about 300 meV, as shown in Fig. 5(a). This result suggest that  $\text{MA}^+$  ions in the  $\alpha$ -phase have a kinetic preference to be arranged in parallel.

For independent rotation in the  $\beta$  phase, as shown in Fig. 5(c), the  $\text{MA}^+$  ion rotates from [001] (RC  $\approx 14$  Å) to about [110] (RC  $\approx 8$  Å), with an energy barrier of 172 meV. If this  $\text{MA}^+$  ion rotates further to [00 $\bar{1}$ ] (RC  $\approx 0$  Å), the total energy barrier is as high as 283 meV. While if the  $\text{MA}^+$  ion was oriented to [00 $\bar{1}$ ] (RC = 0 Å) and the neighbouring  $\text{MA}^+$  ions vectors are [001], the energy barrier is smaller, but still high compared to that of the  $\alpha$  phase. Hence, the energy barrier to flip a  $\text{MA}^+$  ion is 129 meV if the  $\text{MA}^+$  ion is initially anti-parallel to the neighbouring  $\text{MA}^+$  ions, and become as high as 283 meV if the  $\text{MA}^+$  ion is initially parallel to the neighbouring  $\text{MA}^+$  ions. The concerted rotation barrier for one  $\text{MA}^+$  ion is 80–90 meV, which is higher than that (60–70 meV) rotated in the  $\alpha$  phase. We expect collective reorientation to be slower in the  $\beta$  phase in agreement with experiment.<sup>62</sup>

The results show the  $\text{MA}^+$  ions are coupled each other. On one hand, the energy barriers in the  $\alpha$  are lower than those in the  $\beta$  phase, which is likely because the inorganic frame is more compact in the  $\beta$  phase.<sup>16</sup> On the other hand, the energy barriers of independent rotation in the  $\beta$  phase are higher than the energy barrier of collective rotation per  $\text{MA}^+$  ion, which shows that  $\text{MA}^+$  ions kinetically prefer parallel arrangement in both phases.

These low energy barriers also indicate that  $\text{MA}^+$  ion orientation responds to the external field. An energy barrier of 100 meV corresponds to  $9.6 \text{ kJ mol}^{-1}$ , which is in agreement with the low-temperature experimental activation energy  $9.7 \text{ kJ mol}^{-1}$ .<sup>70</sup> The dipole moment of the  $\text{MA}^+$  ion in the gas phase is estimated at  $\mathbf{M} = 2.29 \text{ D}$ , though of course the definition of the dipole moment for a charged species must be chosen.<sup>28</sup> We find a change in polarisation on rotation of the  $\text{MA}^+$  ion from [001] to [110] is about  $\Delta \mathbf{M} \approx 5 \text{ D}$  (shown in Table 7, for four  $\text{MA}^+$  ions, it is 20 D). This includes the response of all the electrons, and the relaxations of the ions described above. The energy change on rotating a dipole by  $90^\circ$  in an electric field  $\mathbf{E}$  is  $|\Delta \mathbf{E}| = |\mathbf{M}| \cdot |\mathbf{E}|$ . The barriers to rotation are not exactly at  $90^\circ$ , but this provides a convenient comparison of energy magnitudes. The field required to change the energy of a 2.29 D dipole by 100 meV on  $90^\circ$  is  $2.1 \times 10^7 \text{ V cm}^{-1}$ , and for a 5 D dipole  $1.0 \times 10^7 \text{ V cm}^{-1}$ . Note that these fields are the 'cavity' fields experienced by the  $\text{MA}^+$  ion or the unit cell. For comparison the fields experienced by the perovskite layer at various times in its history are similar to  $1.0 \text{ V}/300 \text{ nm} = 3.3 \times 10^4 \text{ V cm}^{-1}$ . Here, we assume the probability of a

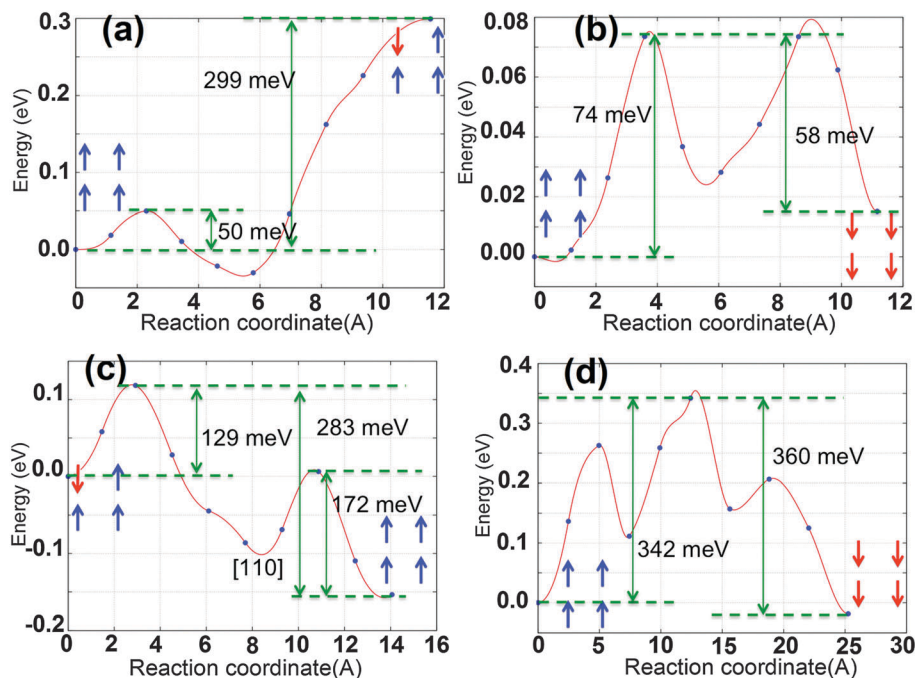


Fig. 5 The energy landscape of  $\text{MA}^+$  ion flip over  $c$  axis in  $\alpha$  and  $\beta$  phase. The energy landscape of independent  $\text{MA}^+$  ion rotation of  $\alpha$  phase (a) and of  $\beta$  phase (c); the energy landscape of collective  $\text{MA}^+$  ion rotation of  $\alpha$  phase (b) and of  $\beta$  phase (d). The energy in (b) is the energy landscape per  $\text{MA}^+$  ion. Arrows in the figure represent  $\text{MA}^+$  orientations.

$\text{MA}^+$  to rotate is the exponential of  $\frac{E_d - E_b}{kT}$ , where  $E_d$  is the energy of dipole moment change,  $E_b$  is the energy barrier and the  $kT$  is its thermal energy. If the energy barrier is 100 meV and  $kT = 25$  meV and  $E_d = 1$  meV for 5 D dipole moment in a field of  $3.3 \times 10^4 \text{ V cm}^{-1}$ , the probability is 1.9%. This is the first point arguing that  $\text{MA}^+$  can rotate under operating field conditions. We conclude that significant electric fields, or sufficient times to overcome barriers, are needed to produce a polarisation that may influence performance.<sup>35,36</sup> This is consistent with the observed slow hysteresis behaviour discussed above.

### 3.9 Polarization, efficiency and hysteresis

We have found above relatively modest changes in electronic structure with  $\text{MA}^+$  ions rotation. This argues against the first possible mechanism, that is, against the possibility that reorientation of the  $\text{MA}^+$  ion affects performance by direct modification of electronic structure. The more likely macroscopic mechanism coupling polarisation to performance is illustrated in Fig. 1. We examine here this macroscopic mechanism, that accumulated charges in charge transport layers can induce a field that hinders charge transport, and that performance is improved when the polarization screens this hindering field, denoted above  $E_0$ . The field produced by the polarization of  $\text{MAPbI}_3$  (red in Fig. 1), together with the capacitive charge (blue in Fig. 1) induced field, will counteract the hindering field, promoting charge transport, and improving PCE. The slow polarisation rates determine slow hysteresis. We examine here the consistency of this mechanism with the observed hysteresis behaviour. Most perovskite solar cells show stronger current-voltage hysteresis when scanning speed

increases,<sup>14,35–38</sup> but Tress *et al.* also observed that slower scanning speed can lead to stronger hysteresis.<sup>14,39</sup>

In the  $\alpha$  phase, the energy differences between the 001-, 110- and 111- $\text{MAPbI}_3$  structures are lower than 20 meV, and the energy barriers for collective  $\text{MA}^+$  ion reorientation are smaller than 100 meV, seen in Table 1. Based on these results, under normal conditions, the  $\text{MA}^+$  ions in the  $\alpha$  phase  $\text{MAPbI}_3$  should be correlated in parallel domains. They are likely disordered overall.<sup>60</sup> For the  $\beta$  phase, both the energy differences and the energy barriers become slightly bigger, so that  $\text{MA}^+$  ions rotate less freely and more slowly. At room temperature, experiment indicates the  $\text{MA}^+$  ion is dynamically disordered,<sup>60–62</sup> but the material is likely ferroelectric.<sup>16–18</sup> Though there are collective, slow fluctuations in the orientations of  $\text{MA}^+$  ions, still a spontaneous polarization state and characteristic ferroelectric hysteresis are seen. The low energy barriers mean that applied fields may promote rearrangement of the  $\text{MA}^+$  ions. As the  $\text{MA}^+$  ions control the dipole moment of the unit cell both in  $\alpha$  and  $\beta$  phase, an external field can tune the polarisation of  $\text{MAPbI}_3$ .

Here we examine whether or not the polarisation field is strong enough to cause hysteresis in hybrid perovskite solar cells. If we take the polarisation difference on  $\text{MA}^+$  rotation ( $\Delta P$ ) as the polarisation (shown in Table 7) induced by a field, then the field should be  $E = \frac{\Delta P}{\epsilon_0(\epsilon_r - 1)} = 3.6 \times 10^8 \text{ V m}^{-1}$ , where  $\epsilon_r$  is the low frequency relative dielectric constant, about 25.<sup>27</sup> This field is about 100 times higher than the hindering field ( $E_0 \approx 3.3 \times 10^6 \text{ V m}^{-1}$ ) under operating conditions. This suggests that only a few  $\text{MA}^+$  ions need be polarised. Assuming  $\text{MA}^+$  ion alignment follows the Boltzmann distribution, the number of

aligned  $\text{MA}^+$  ions is correlated to its potential energy,  $-\mathbf{M} \cdot \mathbf{E}$ , where  $\mathbf{M}$  is the dipole-moment of a  $\text{MA}^+$ . We assume only six orientations (parallel to the field, four perpendicular, and one anti-parallel) are possible. We take the measurement at  $1 \text{ V s}^{-1}$  scanning speed, in ref. 14 Fig. 1a, as an example. At this time scale the trapped charges are able to de-trap, and the capacitive screening field can respond to the hindering field. If the polarised screening field is estimated between  $0.8\text{--}1.6 \times 10^6 \text{ V m}^{-1}$ , then the total field should be between  $E = 12.3$  to  $5.67 \times 10^5 \text{ V m}^{-1}$ . If the total field  $E = 5.67 \times 10^5 \text{ V m}^{-1}$ , then we may roughly estimate an bottom limit on the energy of the polarised  $\text{MA}^+$  ions along these six directions as respectively  $|\mathbf{M}| \cdot |\mathbf{E}|$ , zero and  $-|\mathbf{M}| \cdot |\mathbf{E}|$ . The Boltzmann ratios are then  $\exp(2|\mathbf{M}| \cdot |\mathbf{E}|/kT) : 4 \times \exp(|\mathbf{M}| \cdot |\mathbf{E}|/kT) : 1.00 = 1.005 : 4 \times 1.002 : 1.00$ . The net percentage of the polarised  $\text{MA}^+$  ions is therefore about  $\frac{1.005 - 1.00}{1.005 + 4 \times 1.002 + 1} = 0.08\%$ . The polarised charge density  $\rho$

is about  $6.4 \mu\text{C cm}^{-2} \times 0.07\% = 0.0048 \mu\text{C cm}^{-2}$ . In a parallel-plate capacitor, the field can be estimated as  $E_p = \rho/\epsilon_0\epsilon_r = 2.58 \times 10^5 \text{ V m}^{-1}$ . For the same reason, we can estimated an upper limit of the screening field is about  $5.61 \times 10^5 \text{ V m}^{-1}$ . More calculation details are provided as ESI.† The hindering field is  $2.17 \times 10^6 \text{ V m}^{-1}$ . The mechanism illustrated in Fig. 1 requires that ferroelectric polarisation cancels partly the hindering field. The polarisation changes calculated here are consistent with the mechanism, and we conclude from these calculations that rotation of the  $\text{MA}^+$  ions is likely responsible for the hysteresis and performance characteristics. We note also that the dipole moment is not confined to the  $\text{MA}^+$ , and includes contributions from inorganic ions and electron rearrangement. This is the third point, that polarisation can induce a screening field that agrees with a measured compensating field. This affirms the second mechanism that the polarised field can screen the hindering field, which have illustrated in Fig. 1.

On increase of scanning speed, hysteresis appears when the charge structure cannot relax quickly enough to keep up with the scan, and then disappears when the charge structure changes hardly at all during the scan. The rate of the rotation of  $\text{MA}^+$  ions is low, and when the scanning speed high, the polarisation bound charge cannot respond, so capacitive charge dominates the hysteresis. For such scanning rates, shorter delay times leads to stronger hysteresis, in agreement with experiment.<sup>14,35–38</sup> The capacitive charge relaxation times are usually between 1 ms to 100 ms in silicon based solar cells (around 1 ms) and DSC (around 1–100 ms).<sup>31–34,71</sup> No hysteresis occurs when the delay times are significantly larger than this relaxation.

A long delay time, such as 1 s, eliminates the hysteresis induced by capacitive charges, but  $\text{MA}^+$  ions are still unable to be fully polarised under this delay time due to the large polarisation relaxation time of 1–100 s.<sup>14,38,39,41,44</sup> In this case, the polarisation charges dominate their hysteresis. Hence, for scanning delay times longer than capacitive charge relaxation time, and shorter than the relaxation time of polarisation charges, we expect significant hysteresis in agreement with experiments.<sup>14,39</sup> Fig. 6 shows a measured<sup>14</sup> peak in hysteresis

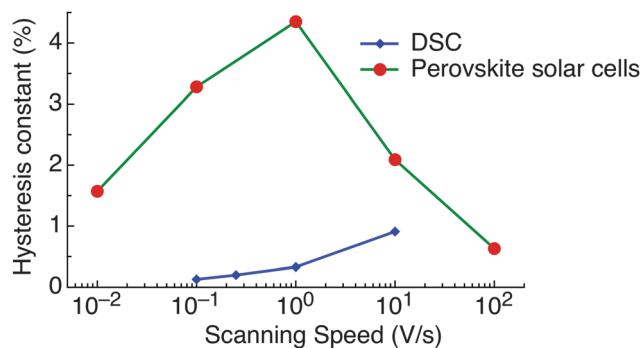


Fig. 6 The dependence of the hysteresis of solar cells' performance and scanning speed. Hysteresis constant is defined as  $\text{PCE}_{\text{max}}^{\text{backward}} - \text{PCE}_{\text{max}}^{\text{forward}}$ . A peak hysteresis is exist when scanning speed increases.

for  $\text{MAPbI}_3$  cells near the relaxation time seen in experiments, at 1 s to 100 s, along with analogous data for a DSC.<sup>31</sup> We conclude that the slower hysteresis, seen to grow with lower scan rates,<sup>14,39</sup> is due to polarisation by reorientation of  $\text{MA}^+$  ions, and the faster hysteresis, seen to grow at higher scan rates, is due to the same capacitive charge build up of electronic excitations that produces hysteresis in a DSC.<sup>14,35–38</sup>

Fig. 1a in the paper by Tress *et al.*<sup>14</sup> shows the current-voltage curve of a hybrid perovskite solar cell, and illustrates the connection between the  $\text{MA}^+$  ion relaxation from one state to another, across the barriers shown above, and PCEs. They start measurement with voltage of 1 V, where the cell is fully polarised in the direction promoting charge transport. For fast scanning,  $10 \text{ V s}^{-1}$  and  $100 \text{ V s}^{-1}$ , the polarisation field is unable to decay. Therefore, higher PCEs occurs with higher scanning speed. When the voltage reaches  $-1 \text{ V}$  and then increase to  $1 \text{ V}$ , for a high scanning speed, the polarisation state is unaltered, so there is no change for its performance. For a slow scan speed, the polarisation state will change, as  $\text{MA}^+$  ions cross the  $\sim 100 \text{ meV}$  barriers, and the hysteresis will be seen, as illustrated in Fig. 6.

## 4 Conclusions

Two possible mechanisms for the influence of polarisation of  $\text{MAPbI}_3$  on photovoltaic performance are examined. We have calculated electronic properties with  $\text{MA}^+$  ions oriented to three representative directions, in phases above and below the phase transition, and the heights of the energy barriers between these structures. We compare collective reorientation of all  $\text{MA}^+$  ions in the crystal, as in a ferroelectric's spontaneous, macroscopic polarisation, to the reorientation of a single  $\text{MA}^+$  ion with its neighbours fixed.

The first possible mechanism is that reorientation of  $\text{MA}^+$  ions directly affects the electronic structure, and so directly affects the creation and transport of electronic excitations. We find only modest changes in band gap, relative permittivity, and most other electronic properties on rotation of  $\text{MA}^+$  ions. We do see that some of the various effective masses that describe the highly anisotropic states at the bottom of the

conduction band change drastically as the  $\text{MA}^+$  ion rotates, but find the overall pattern of effective masses little changes. This allows for the possibility that conduction electron mobility is highly anisotropic, and this anisotropy varies with polarisation state.

The second possible mechanism is that bound charges due to the polarisation of the material, controlled by the collective orientation of  $\text{MA}^+$  ions in part cancels the hindering field due to accumulation of carriers at the transport layers. This ‘macroscopic’ mechanism is illustrated in Fig. 1. The field arising from polarisation, together with that of charge carriers accumulated at the interfaces, counteracts the hindering field, and promotes charge transport. Capacitive charges and polarisation bound charges are also observed in experiment and proved to promote charge transport.<sup>14,43</sup>

We find significant polarisation changes on reorientation of  $\text{MA}^+$  ions. Though not all changes in dipole moment are due to charges on these cations, their configuration does dominate the polarisation. Relaxation of lead ions contributes less than one half of the change produced by  $\text{MA}^+$  ions reorientation. The polarisation changes calculated are large enough to influence charge transport and so performance of a photovoltaic. The rotation energy barrier of a  $\text{MA}^+$  ion, in the  $\alpha$  or  $\beta$  phase of  $\text{MAPbI}_3$ , depends on the orientations of neighbouring  $\text{MA}^+$  ions. If all the  $\text{MA}^+$  ions rotate in concert the barriers are lower than 100 meV per ion. If only one ion rotates with its neighbours fixed, the energy barrier can be as low as 10 meV, but can be as high as 300 meV, depending on the direction of rotation. The  $\text{MA}^+$  ions in  $\text{MAPbI}_3$  prefer to rotate collectively, and to be parallel to their neighbours. These results are consistent with the measured ferroelectricity of the materials.<sup>16–18</sup> We further find that the energy differences between states of different polarisation, and the heights of the energy barriers between different states, are low enough that reorientation is possible under the operating conditions of a photovoltaic with  $\text{MAPbI}_3$  as the absorbing layer, and on relevant time scales.

We interpret the anomalous hysteresis in hybrid perovskite solar cells as due to relaxation of the polarisation field. Based on three points, the compensated field observed in experiment comes from the polarisation of  $\text{MA}^+$  ions. Normal hysteresis, seen for example in a DSC, increases with shorter delay times, due to the relaxation of the capacitive charges accumulated at the interface (including trapping and de-trapping). Both capacitive charges and bound charges play roles in a hybrid perovskite solar cell. For fast scan rates, the polarisation charges are unable to respond. When the delay time is longer than the capacitive charge relaxation time, the discharge or charge of equivalent capacitor is completed with the delay time. Only the polarisation charge lags behind the scanning applied voltage and produces a hysteresis that grows as the scanning rate is reduced.

Taken together with the experimental observation of slow relaxation times, and of hysteresis, our calculations of the  $\text{MA}^+$  rotation energy changes, barrier heights, and polarisation responses show that collective  $\text{MA}^+$  ion rearrangement strongly influences power conversion efficiency.

## Acknowledgements

We thank the National Computational Infrastructure for High Performance Computing resources. We are grateful to the Australian Research Council (DP110103388) and Melbourne Materials Institute for financial support. FH and YBC acknowledge the support of the Australian Centre for Advanced Photovoltaics (ACAP).

## References

- 1 A. Kojima, K. Teshima, Y. Shirai and T. Miyasaka, *J. Am. Chem. Soc.*, 2009, **131**, 6050–6051.
- 2 M. M. Lee, J. Teuscher, T. Miyasaka, T. N. Murakami and H. J. Snaith, *Science*, 2012, **338**, 643–647.
- 3 H.-S. Kim, C.-R. Lee, J.-H. Im, K.-B. Lee, T. Moehl, A. Marchioro, S.-J. Moon, R. Humphry-Baker, J.-H. Yum, J. E. Moser, M. Grätzel and N.-G. Park, *Sci. Rep.*, 2012, **2**, 591.
- 4 Z. Ku, Y. Rong, M. Xu, T. Liu and H. Han, *Sci. Rep.*, 2013, **3**, 3132.
- 5 J. Burschka, N. Pellet, S.-J. Moon, R. Humphry-Baker, P. Gao, M. K. Nazeeruddin and M. Grätzel, *Nature*, 2013, **499**, 316–319.
- 6 P. Docampo, J. M. Ball, M. Darwich, G. E. Eperon and H. J. Snaith, *Nat. Commun.*, 2013, **4**, 2761.
- 7 G. Hodes, *Science*, 2013, **342**, 317–318.
- 8 M. Liu, M. B. Johnston and H. J. Snaith, *Nature*, 2013, **501**, 395–398.
- 9 H. Zhou, Q. Chen, G. Li, S. Luo, T.-b. Song, H.-S. Duan, Z. Hong, J. You, Y. Liu and Y. Yang, *Science*, 2014, **345**, 542–546.
- 10 F. Brivio, A. B. Walker and A. Walsh, *APL Mater.*, 2013, **1**, 042111.
- 11 J. M. Frost, K. T. Butler and A. Walsh, *APL Mater.*, 2014, **2**, 081506.
- 12 F. Brivio, K. T. Butler, A. Walsh and M. van Schilfgaarde, *Phys. Rev. B: Condens. Matter Mater. Phys.*, 2014, **89**, 155204.
- 13 C. Quarti, E. Mosconi and F. De Angelis, *Chem. Mater.*, 2014, **26**, 6557–6569.
- 14 W. Tress, N. Marinova, T. Moehl, S. M. Zakeeruddin, M. K. Nazeeruddin and M. Grätzel, *Energy Environ. Sci.*, 2015, **8**, 995–1004.
- 15 V. W. Bergmann, S. a. L. Weber, F. Javier Ramos, M. K. Nazeeruddin, M. Grätzel, D. Li, A. L. Domanski, I. Lieberwirth, S. Ahmad and R. Berger, *Nat. Commun.*, 2014, **5**, 5001.
- 16 C. C. Stoumpos, C. D. Malliakas and M. G. Kanatzidis, *Inorg. Chem.*, 2013, **52**, 9019–9038.
- 17 Y. Kutes, L. Ye, Y. Zhou, S. Pang, B. D. Huey and N. P. Padture, *J. Phys. Chem. Lett.*, 2014, **5**, 3335–3339.
- 18 P. Zhao, J. Xu, C. Ma, W. Ren, L. Wang, L. Bian and A. Chang, *Scr. Mater.*, 2015, **102**, 51–54.
- 19 J. Huang, H. Jia, L. Li, Z. Lu, W. Zhang, W. He, B. Jiang, A. Tang, Z. Tan, C. Zhan, Y. Li and J. Yao, *Phys. Chem. Chem. Phys.*, 2012, **14**, 14238–14242.
- 20 C. K. Song, A. C. White, L. Zeng, B. J. Leever, M. D. Clark, J. D. Emery, S. J. Lou, A. Timalisina, L. X. Chen, M. J. Bedzyk and T. J. Marks, *ACS Appl. Mater. Interfaces*, 2013, **5**, 9224–9240.



- 21 Q. Liu, I. Khatri, R. Ishikawa, a. Fujimori, K. Ueno, K. Manabe, H. Nishino and H. Shirai, *Appl. Phys. Lett.*, 2013, **103**, 163503.
- 22 Y. Yuan, P. Sharma, Z. Xiao, S. Poddar, A. Gruverman, S. Ducharme and J. Huang, *Energy Environ. Sci.*, 2012, **5**, 8558.
- 23 Y.-C. Hsiao, H. Zang, I. Ivanov, T. Xu, L. Lu, L. Yu and B. Hu, *J. Appl. Phys.*, 2014, **115**, 154506.
- 24 G. Xing, N. Mathews, S. Sun, S. S. Lim, Y. M. Lam, M. Grätzel, S. Mhaisalkar, T. C. Sum and M. Gratzel, *Science*, 2013, **342**, 344–347.
- 25 S. D. Stranks, G. E. Eperon, G. Grancini, C. Menelaou, M. J. P. Alcocer, T. Leijtens, L. M. Herz, A. Petrozza and H. J. Snaith, *Science*, 2013, **342**, 341–344.
- 26 Y. Wang, T. Gould, J. F. Dobson, H. Zhang, H. Yang, X. Yao and H. Zhao, *Phys. Chem. Chem. Phys.*, 2013, **16**, 1424–1429.
- 27 M. H. Du, *J. Mater. Chem. A*, 2014, **2**, 9091.
- 28 J. M. Frost, K. T. Butler, F. Brivio, C. H. Hendon, M. van Schilfgaarde and A. Walsh, *Nano Lett.*, 2014, **14**, 2584–2590.
- 29 S. Liu, F. Zheng, N. Z. Koocher, H. Takenaka, F. Wang and A. M. Rappe, *J. Phys. Chem. Lett.*, 2015, **6**, 693–699.
- 30 F. Zheng, H. Takenaka, F. Wang, N. Z. Koocher and A. M. Rappe, *J. Phys. Chem. Lett.*, 2015, **6**, 31–37.
- 31 N. Koide and L. Han, *Rev. Sci. Instrum.*, 2004, **75**, 2828.
- 32 N. Koide, Y. Chiba and L. Han, *Jpn. J. Appl. Phys.*, 2005, **44**, 4176–4181.
- 33 M. Herman, M. Jankovec and M. Topič, *Int. J. Photoenergy*, 2012, **2012**, 1–11.
- 34 W. Brütting, *Physics of Organic Semiconductors*, Wiley-VCH Verlag GmbH & Co. KGaA, Weinheim, FRG, 2005, p. 273.
- 35 M. Xiao, F. Huang, W. Huang, Y. Dkhissi, Y. Zhu, J. Etheridge, A. Gray-Weale, U. Bach, Y.-B. Cheng and L. Spiccia, *Angew. Chem., Int. Ed.*, 2014, **53**, 9898–9903.
- 36 F. Huang, Y. Dkhissi, W. Huang, M. Xiao, I. Benesperi, S. Rubanov, Y. Zhu, X. Lin, L. Jiang, Y. Zhou, A. Gray-Weale, J. Etheridge, C. R. McNeill, R. a. Caruso, U. Bach, L. Spiccia and Y.-B. Cheng, *Nano Energy*, 2014, **10**, 10–18.
- 37 J.-W. Lee, D.-J. Seol, A.-N. Cho and N.-G. Park, *Adv. Mater.*, 2014, **6**, 4991–4998.
- 38 R. S. Sanchez, V. Gonzalez-Pedro, J.-W. Lee, N.-G. Park, Y. S. Kang, I. Mora-Sero and J. Bisquert, *J. Phys. Chem. Lett.*, 2014, **5**, 2357–2363.
- 39 H. J. Snaith, A. Abate, J. M. Ball, G. E. Eperon, T. Leijtens, N. K. Noel, S. D. Stranks, J. T.-w. Wang, K. Wojciechowski and W. Zhang, *J. Phys. Chem. Lett.*, 2014, **5**, 1511–1515.
- 40 J. Wei, Y. Zhao, H. Li, G. Li, J. Pan, D. Xu, Q. Zhao and D. Yu, *J. Phys. Chem. Lett.*, 2014, **5**, 3937–3945.
- 41 H.-S. Kim and N.-G. Park, *J. Phys. Chem. Lett.*, 2014, **5**, 2927–2934.
- 42 N. J. Jeon, J. H. Noh, Y. C. Kim, W. S. Yang, S. Ryu and S. I. Seok, *Nat. Mater.*, 2014, **13**, 897–903.
- 43 Y. Zhang, M. Liu, G. E. Eperon, T. C. Leijtens, D. McMeekin, M. Saliba, W. Zhang, M. de Bastiani, A. Petrozza, L. M. Herz, M. B. Johnston, H. Lin and H. J. Snaith, *Mater. Horiz.*, 2015, **1**, 96.
- 44 R. Gottesman, E. Haltzi, L. Gouda, S. Tirosh, Y. Bouhadana, A. Zaban, E. Mosconi and F. De Angelis, *J. Phys. Chem. Lett.*, 2014, **5**, 2662–2669.
- 45 G. Kresse and J. Furthmüller, *Comput. Mater. Sci.*, 1996, **6**, 15–50.
- 46 G. Kresse, J. Furthmüller and J. Furthmüller, *Phys. Rev. B: Condens. Matter Mater. Phys.*, 1996, **54**, 11169–11186.
- 47 P. E. Blöchl, *Phys. Rev. B: Condens. Matter Mater. Phys.*, 1994, **50**, 17953–17979.
- 48 G. Giorgi, J.-i. Fujisawa, H. Segawa and K. Yamashita, *J. Phys. Chem. C*, 2014, **118**, 12176–12183.
- 49 G. Giorgi, J.-I. Fujisawa, H. Segawa and K. Yamashita, *J. Phys. Chem. Lett.*, 2013, **4**, 4213–4216.
- 50 P. Umari, E. Mosconi and F. De Angelis, *Sci. Rep.*, 2014, **4**, 4467.
- 51 X. Wu, M. C. Vargas, S. Nayak, V. Lotrich and G. Scoles, *J. Chem. Phys.*, 2001, **115**, 8748–8757.
- 52 J. P. Perdew, A. Ruzsinszky, G. I. Csonka, O. A. Vydrov, G. E. Scuseria, L. A. Constantin, X. Zhou and K. Burke, *Phys. Rev. Lett.*, 2008, **100**, 136406.
- 53 D. Vanderbilt and R. D. King-Smith, *Phys. Rev. B: Condens. Matter Mater. Phys.*, 1993, **48**, 4442–4455.
- 54 R. Resta, *Ferroelectrics*, 1992, **136**, 51–55.
- 55 R. Resta, *Rev. Mod. Phys.*, 1994, **66**, 899–915.
- 56 R. D. King-Smith and D. Vanderbilt, *Phys. Rev. B: Condens. Matter Mater. Phys.*, 1993, **47**, 1651–1654.
- 57 X. Wu, D. Vanderbilt and D. Hamann, *Phys. Rev. B: Condens. Matter Mater. Phys.*, 2005, **72**, 035105.
- 58 G. Mills, H. Jónsson and G. K. Schenter, *Surf. Sci.*, 1995, **324**, 305–337.
- 59 G. Henkelman, B. P. Uberuaga and H. Jónsson, *J. Chem. Phys.*, 2000, **113**, 9901.
- 60 T. Baikie, Y. Fang, J. M. Kadro, M. Schreyer, F. Wei, S. G. Mhaisalkar, M. Graetzel and T. J. White, *J. Mater. Chem. A*, 2013, **1**, 5628.
- 61 Y. Kawamura, H. Mashiyama and K. Hasebe, *J. Phys. Soc. Jpn.*, 2002, **71**, 1694–1697.
- 62 R. E. Wasylshen, O. Knop and J. B. Macdonald, *Solid State Commun.*, 1985, **56**, 581–582.
- 63 J. Even, L. Pedesseau, E. Tea, S. Almosni, A. Rolland, C. Robert, J.-M. Jancu, C. Cornet, C. Katan, J.-F. Guillemoles and O. Durand, *Int. J. Photoenergy*, 2014, **2014**, 1–11.
- 64 J. Even, L. Pedesseau, J.-M. Jancu and C. Katan, *J. Phys. Chem. Lett.*, 2013, **4**, 2999–3005.
- 65 I. Borriello, G. Cantele and D. Ninno, *Phys. Rev. B: Condens. Matter Mater. Phys.*, 2008, **77**, 235214.
- 66 M. H. Du and D. J. Singh, *Phys. Rev. B: Condens. Matter Mater. Phys.*, 2010, **81**, 1–5.
- 67 M. Hirasawa, T. Ishihara, T. Goto, K. Uchida and N. Miura, *Phys. B*, 1994, **201**, 427–430.
- 68 T. Ishihara, *J. Lumin.*, 1994, **60–61**, 269–274.
- 69 K. Tanaka, T. Takahashi, T. Ban, T. Kondo, K. Uchida and N. Miura, *Solid State Commun.*, 2003, **127**, 619–623.
- 70 N. Onoda-Yamamuro, T. Matsuo and H. Suga, *J. Phys. Chem. Solids*, 1992, **53**, 935–939.
- 71 N. Taylor, *PV Power Measurement Compiled by Partners in the Performance FP6 Integrated Project*, JRC Scientific and Technical Report EUR, Luxembourg, 2010.